New Journal of Physics
The open access journal at the forefront of physics

Deutsche Physikalische Gesellschaft DPG
IOP Institute of Physics

Published in partnership with: Deutsche Physikalische Gesellschaft and the Institute of Physics

Check for updates

PAPER

A field-quadrature perspective on strong-field ionization with squeezed light

Haoyu Liu[1,*], **Jianmin Yuan**[1,2,*] and **Xu Wang**[1,*]

[1] Graduate School, China Academy of Engineering Physics, Beijing 100193, People's Republic of China
[2] Institute of Atomic and Molecular Physics, Jilin University, Changchun 130012, People's Republic of China
[*] Authors to whom any correspondence should be addressed.

E-mail: liuhaoyu21@gscaep.ac.cn, jmyuan@gscaep.ac.cn and xwang@gscaep.ac.cn

Keywords: strong-field ionization, bright squeezed vacuum, field quadratures

OPEN ACCESS

RECEIVED
12 August 2026

REVISED
23 September 2026

ACCEPTED FOR PUBLICATION
7 October 2026

PUBLISHED
23 October 2026

Original content from this work may be used under the terms of the Creative Commons Attribution 4.0 licence.

Any further distribution of this work must maintain attribution to the author(s) and the title of the work, journal citation and DOI.

Abstract

Bright squeezed vacuum (BSV) has emerged as a macroscopic nonclassical light source capable of driving strong-field processes. Yet its broad, long-tailed photon-number distribution bears little resemblance to the narrow poissonian distribution of a coherent field, obscuring how the corresponding strong-field responses are connected. We show that field-quadrature space supplies the missing continuous description: coherent, squeezed coherent, and BSV states are Gaussian wave packets distinguished only by their centers and widths. This representation provides a unified framework for tracing the coherent-to-BSV transition at fixed mean photon number and for analyzing both ionization yields and photoelectron spectra. Crucially, BSV is a symmetry-protected endpoint in quadrature space. Near the BSV limit, we identify a simple scaling law of the ionization response associated with a residual coherent component. We show that this scaling arises from parity-induced stationarity with respect to the Gaussian center, together with the accompanying width variation near the BSV limit. The result provides a symmetry-based criterion for approaching the BSV regime and a potential probe of a mode-matched coherent displacement through the strong-field response itself.

1. Introduction

Strong-field ionization [1–6] is a paradigmatic nonlinear and nonperturbative response of matter to intense light. It is conventionally studied with intense coherent laser fields, the relative quantum fluctuations of which are negligible and can therefore be treated classically. Within this semiclassical framework, approximate methods like the Keldysh–Faisal–Reiss theory [7–9] and the Ammosov–Delone–Krainov theory [10] have been developed to describe the ionization process, while recollision models further explain characteristic structures in photoelectron spectra [11–13].

Recent advances in bright squeezed vacuum (BSV) sources [14–16] have opened a regime in which macroscopic nonclassical light participates directly in strong-field dynamics [17–22]. Unlike weak quantum-light sources, BSV combines a large mean photon number with strong nonclassical fluctuations. This combination has motivated studies of electron motion [23–26], ionization [27–32], and high-harmonic generation [17, 33–37] driven by squeezed-vacuum fields. Previous studies of strong-field ionization have established that the quantum properties of the light field can modify ionization probabilities and photoelectron interference structures [27], reshape high-order above-threshold-ionization spectra and their cutoff energies [28, 31, 32], and affect photoelectron number statistics [29]. These studies primarily characterized how specific quantum states of light affect ionization observables. Many of these studies employ phase-space approaches, most commonly Husimi-type distributions, in which quantum-light-driven strong-field observables are represented as a superposition of coherent-state (classical-field) responses. This viewpoint has been useful for incorporating the broad intensity fluctuations of squeezed-vacuum states. At the level of physical interpretation, however, the resulting behavior is often discussed in terms of photon-number statistics: coherent light has a narrow poissonian distribution whereas BSV

© 2026 The Author(s). Published by IOP Publishing Ltd on behalf of the Institute of Physics and Deutsche Physikalische Gesellschaft

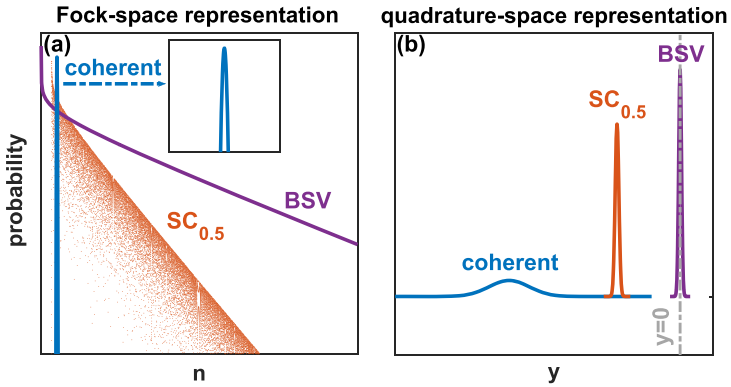


Figure 1. Coherent-to-BSV transition in complementary representations. (a) In Fock space, coherent light, the squeezed coherent state $SC_{0.5}$, and BSV have qualitatively different photon-number distributions. The inset enlarges the coherent-state distribution around its mean photon number to show its finite poissonian width. (b) In field-quadrature space, the same states are Gaussian wave packets whose centers and widths vary continuously; BSV is centered at $y = 0$. The probability is displayed on a logarithmic scale in (a) and on a linear scale in (b).

has a broad, long-tailed distribution [17, 18, 29, 38]. The two endpoints appear qualitatively disconnected, and the photon-number picture does not expose which change in the quantum state controls the approach of a strong-field observable to its BSV value.

The purpose of the present work is not to further quantify how much the ionization responses differ between the coherent and BSV endpoints, but to use the field-quadrature representation [38–40] to provide a continuous description of the coherent-to-BSV transition and reveal how ionization observables evolve along this transition. In this representation, coherent, squeezed coherent (SC), and BSV states are described as Gaussian wave packets: the coherent component determines the wave-packet center, whereas the squeezing determines the width [40, 41]. The coherent-to-BSV transition can therefore be described as a continuous change in the two parameters (y_0, σ^2), even though their photon-number distributions look qualitatively different [42, 43]. Moreover, BSV is identified geometrically as the centered point $y_0 = 0$. This makes the action of field parity explicit and allows the response to a residual coherent displacement to be classified by symmetry. Figure 1 contrasts the photon-number and quadrature descriptions for representative states along this transition.

We study a family of SC states that connects coherent light continuously to BSV while keeping the mean photon number fixed. The redistribution of photons between coherent component and squeezing is parameterized by $\chi = N_{\mathrm{sq}}/N_{\mathrm{coh}}$. Along this path, we calculate the total ionization yield and the photoelectron energy spectrum and interpret their evolution through the Gaussian center and width. At the BSV endpoint, combined atom-field parity makes every parity-even ionization observable an even function of y_0. The endpoint is therefore stationary against coherent displacement, and the leading center correction is quadratic. For observables that are smooth in (y_0, σ^2) near BSV, this constraint and the simultaneous width correction produce the leading scaling $O(\chi) - O_{\mathrm{BSV}} \propto (1+\chi)^{-1}$. The scaling is thus a consequence of symmetry and the specified path, rather than an empirical fitting law. These results yield a simple near-BSV scaling that may help identify the BSV regime and diagnose a residual mode-matched coherent component by monitoring the strong-field ionization response itself, rather than by performing a direct optical quadrature measurement.

The remainder of this article is organized as follows. Section 2 introduces the field-quadrature formulation of quantum light-atom interactions and the corresponding expressions for the ionization yield and photoelectron spectrum. Section 3 presents the ionization yield and photoelectron spectra along the coherent-to-BSV transition and analyzes their evolution in terms of the Gaussian center and width, leading to the near-BSV endpoint scaling. Section 4 discusses the applicability and possible experimental implication of this scaling. Conclusions are given in section 5.

2. Methods

2.1. Quantum light-atom interaction

The Hamiltonian of the coupled single-electron atom and single-mode light field is taken as $\hat{H}(t) = \hat{H}_{\mathrm{A}} + \hat{H}_{\mathrm{F}} + \hat{H}_{\mathrm{int}}(t)$, where $\hat{H}_{\mathrm{A}}$ is the atomic Hamiltonian and $\hat{H}_{\mathrm{F}} = \omega \hat{a}^{\dagger}\hat{a}$ describes the quantized field, with ω denoting the angular frequency of the driving mode. Assuming that the field polarization is

aligned with the atomic dipole, the interaction Hamiltonian takes the form $\hat{H}_{\rm int}(t) = -f(t)\hat{d}\hat{E}$, where $f(t)$ is an envelope function. An exact quantum description of a finite-duration optical pulse generally involves a finite bandwidth and hence many frequency modes. In the present effective single-mode model, the nonclassical quantum state is assigned to the selected mode, while $f(t)$ retains the finite-pulse character of the interaction without introducing additional quantized field degrees of freedom. Similar envelope-based single-mode treatments have been used in [44, 45]. Here, $\hat{d}$ is the dipole operator, and $\hat{E} = \mathrm{i}\epsilon^{(1)}(\hat{a} - \hat{a}^\dagger)$ is the electric-field operator. Here, $\epsilon^{(1)} = \sqrt{\omega/(2\epsilon_0 V)}$ is the single-photon field amplitude, V is the quantization volume [46–48], and ϵ_0 is the vacuum permittivity.

We introduce the canonical light-field quadrature operators [38, 39], $\hat{y} = (\hat{a}^\dagger + \hat{a})/\sqrt{2\omega}$ and $\hat{p}_y = \mathrm{i}\sqrt{\omega/2}(\hat{a}^\dagger - \hat{a})$. The initial light state is taken to be a real displaced squeezed state, $|\alpha_0, r\rangle = \hat{D}(\alpha_0)\hat{S}(r)|0\rangle$, with real coherent parameter α_0 and real squeezing parameter r. Here, $\hat{D}(\alpha_0) = \exp(\alpha_0\hat{a}^\dagger - \alpha_0\hat{a})$ is the displacement operator, and $\hat{S}(r) = \exp[\frac{r}{2}(\hat{a}^2 - \hat{a}^{\dagger 2})]$ is the squeezing operator.

In the field-quadrature representation, $\hat{y}|y\rangle = y|y\rangle$, this state has the Gaussian wave function

$$\langle y|\alpha_0, r\rangle \equiv \varphi_{y_0,\sigma}(y) = \left(\pi\sigma^2\right)^{-1/4} \exp\left[-\frac{(y-y_0)^2}{2\sigma^2}\right]. \tag{1}$$

The Gaussian center $y_0 = \sqrt{2/\omega}\,\alpha_0$ is determined by the coherent parameter, whereas the wave-function width $\sigma = \mathrm{e}^{-r}/\sqrt{\omega}$ is controlled by the squeezing parameter. Along the coherent-to-BSV path considered here, the mean photon number $N = \alpha_0^2 + \sinh^2 r = N_{\rm coh} + N_{\rm sq}$ is held fixed. All fields on this path therefore have the same intensity $I = c\omega N/V = \epsilon_0 c|E|^2/2$, where c is the speed of light and $|E| = \sqrt{2\omega N/(\epsilon_0 V)}$ is the corresponding effective field amplitude [38]. The coherent-state limit has $r = 0$, whereas the BSV limit has $\alpha_0 = 0$ and $r > 0$. As introduced above, the redistribution is quantified by the relative squeezing ratio $\chi = N_{\rm sq}/N_{\rm coh} = \sinh^2 r/\alpha_0^2$. Thus, $\chi = 0$ for the coherent state and $\chi \to \infty$ for BSV. At fixed N, $N_{\rm coh} = N/(1+\chi)$ and $N_{\rm sq} = N\chi/(1+\chi)$.

From equation (1), the initial light-atom state is therefore written as

$$|\Psi(0; y_0, \sigma)\rangle = |g\rangle \otimes |\alpha_0, r\rangle = \int \mathrm{d}y\, \varphi_{y_0,\sigma}(y)\, |g, y\rangle, \tag{2}$$

where $|g\rangle$ is the electronic ground state and $|g, y\rangle \equiv |g\rangle \otimes |y\rangle$. After an interaction time t_e, the state becomes

$$\begin{aligned} |\Psi(t_e; y_0, \sigma)\rangle &= \hat{U}(t_e, 0)\, |\Psi(0; y_0, \sigma)\rangle \\ &= \int \mathrm{d}y\, \varphi_{y_0,\sigma}(y)\, |\Phi_y(t_e)\rangle, \end{aligned} \tag{3}$$

where $|\Phi_y(t_e)\rangle \equiv \hat{U}(t_e, 0)|g, y\rangle$ and $\hat{U}(t_e, 0) = \hat{T}\exp\left[-\mathrm{i}\int_0^{t_e} \hat{H}(t)\,\mathrm{d}t\right]$ is the time-evolution operator, with $\hat{T}$ denoting the time-ordering operator. Although $f(t)$ is not displayed explicitly in the subsequent expressions, it remains included through the time-ordered propagator $\hat{U}(t_e, 0)$. The electronic reduced density matrix is obtained by tracing over the field degree of freedom [40],

$$\begin{aligned} \hat{\rho}_{\rm A}(t_e; y_0, \sigma) &= \mathrm{Tr}_{\rm F}\left[|\Psi(t_e; y_0, \sigma)\rangle\langle\Psi(t_e; y_0, \sigma)|\right] \\ &= \int \mathrm{d}y_1 \mathrm{d}y_2\, \varphi_{y_0,\sigma}(y_1)\, \varphi^*_{y_0,\sigma}(y_2)\, \hat{\mathcal{R}}(y_1, y_2; t_e), \end{aligned} \tag{4}$$

where

$$\hat{\mathcal{R}}(y_1, y_2; t_e) = \mathrm{Tr}_{\rm F}\left[|\Phi_{y_1}(t_e)\rangle\langle\Phi_{y_2}(t_e)|\right]. \tag{5}$$

Equation (4) shows that the final electronic state is determined by a quadrature-space kernel weighted by the initial Gaussian field wave packet.

2.2. Ionization yield and photoelectron spectrum

We next define the ionization observables from the reduced electronic density matrix in equation (4). Let $\{|\phi_\nu\rangle\}$ be the bound eigenstates of the field-free atomic Hamiltonian $\hat{H}_{\rm A}$. The projector onto the bound electronic subspace is $\hat{P}_{\rm B} = \sum_{\nu\in{\rm bound}} |\phi_\nu\rangle\langle\phi_\nu|$, and the corresponding projector onto the ionized subspace is $\hat{Q}_{\rm B} = \hat{I}_{\rm A} - \hat{P}_{\rm B}$, where $\hat{I}_{\rm A}$ is the identity operator in the electronic Hilbert space.

The total ionization yield is defined as the population outside the bound subspace,

$$Y_{\rm ion}(y_0, \sigma) = \mathrm{Tr}_{\rm A}\left[\hat{Q}_{\rm B}\hat{\rho}_{\rm A}(t_e; y_0, \sigma)\right]. \tag{6}$$

Substituting equation (4) into equation (6), the yield can be written in the quadrature-kernel form

$$Y_{\mathrm{ion}}(y_0,\sigma) = \int \mathrm{d}y_1 \mathrm{d}y_2\, \varphi_{y_0,\sigma}(y_1)\, \varphi^*_{y_0,\sigma}(y_2)\, K_{\mathrm{ion}}(y_1,y_2;t_e)\,, \tag{7}$$

where $K_{\mathrm{ion}}(y_1,y_2;t_e) = \mathrm{Tr}_{\mathrm{A}}\left[\hat{Q}_{\mathrm{B}}\hat{\mathcal{R}}(y_1,y_2;t_e)\right]$. Thus, $K_{\mathrm{ion}}(y_1,y_2;t_e)$ represents the ionization response associated with the two initial field-quadrature components y_1 and y_2, while the Gaussian factors specify how this response is averaged over the initial quantum light state.

The photoelectron energy spectrum is obtained by first removing the bound electronic components and then resolving the energy of the remaining continuum part. Formally, the energy-resolved measurement involves $\delta(E_k - \hat{H}_{\mathrm{A}})$. In numerical calculations, the continuum is represented by a finite set of box-discretized states. We therefore replace the delta function by a finite-width energy-window operator [49–51],

$$\hat{W}^{(q)}_{E_k} = \frac{\gamma^{2q}}{\left[\left(E_k - \hat{H}_{\mathrm{A}}\right)^2 + \gamma^2\right]^q}, \tag{8}$$

where E_k is the center of the energy window, γ controls the energy resolution, and q is the order of the window. In the present calculations, we use $\gamma = 0.01$ a.u. and $q = 2$. The photoelectron energy spectrum is then defined as

$$P(E_k;y_0,\sigma) = \mathrm{Tr}_{\mathrm{A}}\left[\hat{Q}_{\mathrm{B}}\hat{W}^{(q)}_{E_k}\hat{Q}_{\mathrm{B}}\hat{\rho}_{\mathrm{A}}(t_e;y_0,\sigma)\right]. \tag{9}$$

Using the quadrature form of the reduced density matrix, this becomes

$$P(E_k;y_0,\sigma) = \int \mathrm{d}y_1 \mathrm{d}y_2\, \varphi_{y_0,\sigma}(y_1)\, \varphi^*_{y_0,\sigma}(y_2)\, K_{E_k}(y_1,y_2;t_e)\,, \tag{10}$$

where the energy-resolved response kernel is $K_{E_k}(y_1,y_2;t_e) = \mathrm{Tr}_{\mathrm{A}}\left[\hat{Q}_{\mathrm{B}}\hat{W}^{(q)}_{E_k}\hat{Q}_{\mathrm{B}}\hat{\mathcal{R}}(y_1,y_2;t_e)\right]$. Equation (10) shows that the photoelectron spectrum admits a quadrature-kernel representation analogous to that of the total ionization yield.

For the numerical implementation, we use a one-dimensional soft-core model [52, 53], $\hat{H}_{\mathrm{A}} = \hat{p}_x^2/2 - 1/\sqrt{\hat{x}^2+\nu^2}$, where $\hat{x}$ and $\hat{p}_x$ are the electron position and momentum operators. The soft-core parameter is chosen as $\nu^2 = 2$, giving a ground-state energy of -0.5 a.u., close to the ionization potential of the hydrogen atom. The electronic coordinate is represented using a common grid spacing of $\Delta x = 0.45$ a.u. For the 400-nm four-cycle, 400-nm eight-cycle, and 600-nm four-cycle calculations, the spatial ranges are $x \in [-700, 700]$, $[-1167, 1167]$, and $[-933, 933]$ a.u., respectively. No absorbing boundary is used in these calculations. For the quantum light field, the field-quadrature representation is used for the analytical formulation and physical interpretation. The calculated observables are independent of the choice of field representation. In the numerical calculations, the mean photon number is fixed at $N = 10000$, and the photon-number cutoff is set to $N_{\mathrm{F}} = 150000$. Similar numerical approaches that keep the mean photon number fixed have previously been employed in [54–56].

3. Results and discussions

We now follow the ionization response along the fixed-N coherent-to-BSV path. We first present the ionization yield and the photoelectron energy spectrum, then examine their endpoint behavior, and finally relate both observables to the continuous evolution of the Gaussian center and width in quadrature space.

3.1. Ionization yield and photoelectron spectrum along the coherent-to-BSV transition

Figure 2 shows the ionization yield as χ increases along the coherent-to-BSV path. Panels (a) and (b) correspond to $I = 1\times10^{14}\,\mathrm{W\,cm^{-2}}$ and $5\times10^{13}\,\mathrm{W\,cm^{-2}}$, respectively. At both intensities, the yield changes rapidly up to approximately $\chi = 8$ and then approaches its BSV value more slowly. The direction of the change is intensity dependent: the yield decreases with χ in the higher intensity case but increases in the lower intensity case. This behavior is consistent with earlier results that BSV field fluctuations can enhance ionization at lower intensities, whereas ionization saturation limits that enhancement at higher intensities [29, 30].

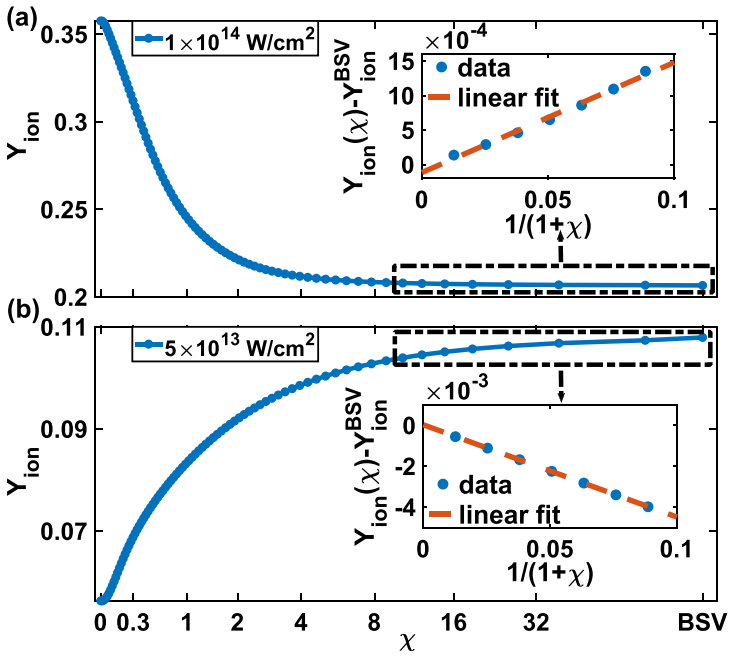


Figure 2. Total ionization yield as a function of the relative squeezing ratio χ along the coherent-to-BSV transition at fixed mean photon number. (a) and (b) correspond to $I = 1 \times 10^{14}\,\mathrm{W\,cm^{-2}}$ and $5 \times 10^{13}\,\mathrm{W\,cm^{-2}}$, respectively. For visual clarity, the main horizontal axis is plotted using the transformed coordinate $\log_{10}(1+\chi)$, with tick labels indicating the corresponding values of χ; the BSV point is shown separately as the endpoint. The insets show the near-BSV deviation $Y_{\mathrm{ion}}(\chi) - Y_{\mathrm{ion}}^{\mathrm{BSV}}$ plotted as a function of $1/(1+\chi)$. Dashed lines denote linear fits in the endpoint region. The driving pulse has a central wavelength of 400 nm and a duration of four optical cycles, with a trapezoidal envelope consisting of a one-cycle ramp-on, a two-cycle plateau, and a one-cycle ramp-off. The BSV limit corresponds to $\chi \to \infty$.

Despite the opposite trends, both data sets approach the BSV value approximately linearly in $1/(1+\chi)$ over the displayed endpoint range. The insets plot $Y_{\mathrm{ion}}(\chi) - Y_{\mathrm{ion}}^{\mathrm{BSV}}$ against this variable. The slopes have opposite signs, but the leading power is the same. Section 3.2 derives this endpoint power for smooth parity-even observables; the wider numerical range over which linearity remains accurate depends on the size of higher-order corrections.

Figure 3 shows the photoelectron energy spectra along the coherent-to-BSV transition. Figures 3(a) and (b) correspond to $I = 1 \times 10^{14}\,\mathrm{W\,cm^{-2}}$ and $5 \times 10^{13}\,\mathrm{W\,cm^{-2}}$, respectively. In both cases, the photoelectron spectra exhibit a series of nearly equally spaced above-threshold ionization (ATI) structures over a broad range of electron energies. Although the total ionization yield changes in opposite directions at the two intensities, the spectra show a common trend as the driving state approaches the BSV limit: higher-order ATI peaks become more pronounced. This behavior is consistent with previous studies [28, 29] and may be related to the superbunching-induced enhancement of multiphoton pathways [57] in BSV-driven processes. The horizontal dashed lines mark the ATI energies used below for the energy-resolved trend and endpoint scaling analysis.

Figure 4 shows the χ dependence of the selected ATI energy signals marked in figure 3. Figures 4(a) and (b) correspond to $I = 1 \times 10^{14}\,\mathrm{W\,cm^{-2}}$, while figures 4(c) and (d) correspond to $I = 5 \times 10^{13}\,\mathrm{W\,cm^{-2}}$. The energy-resolved signals change rapidly at smaller χ and then vary more gradually as the BSV side is approached, showing a smooth coherent-to-BSV transition similar to that observed in the total ionization yield. To examine how these signals approach the BSV value, the insets plot the deviation $P(E_k;\chi) - P(E_k;\mathrm{BSV})$ as a function of $1/(1+\chi)$. Across the representative ATI energy channels displayed here, the deviations are approximately linear over the range close to the BSV side. This numerical linearity indicates that the same finite-range behavior observed in the total ionization yield also appears at the level of the energy-resolved photoelectron spectrum. The slopes and magnitudes depend on the selected energy and on the intensity.

This evolution also provides a physical picture of the electron dynamics along the coherent-to-BSV transition. At fixed mean photon number, increasing χ continuously reduces the coherent component and increases the squeezed component. The electron dynamics therefore changes from being dominated by the coherent mean field to receiving an increasing contribution from electric-field fluctuations. As

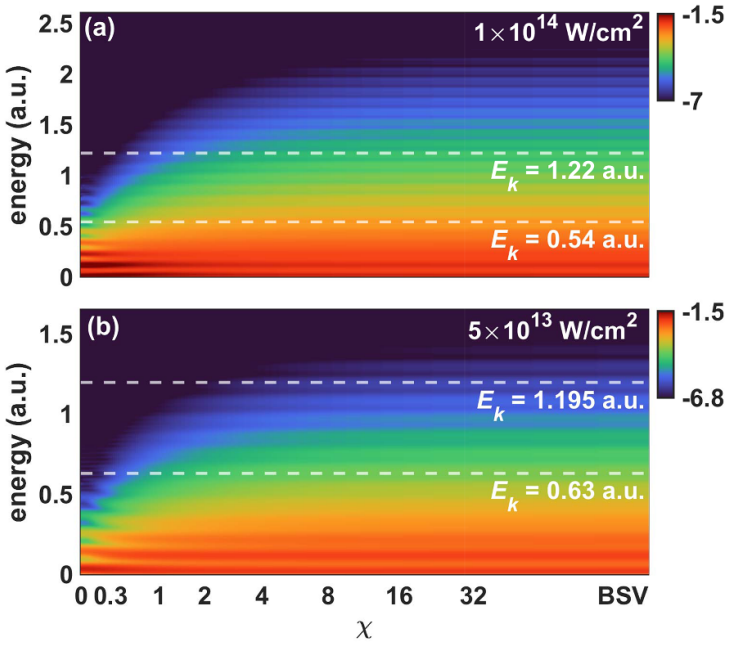


Figure 3. Photoelectron energy spectra as a function of the relative squeezing ratio χ along the coherent-to-BSV transition at fixed mean photon number. (a) and (b) correspond to $I = 1 \times 10^{14}\,\mathrm{W\,cm^{-2}}$ and $5 \times 10^{13}\,\mathrm{W\,cm^{-2}}$, respectively. The color scale represents $\log_{10} P(E_k;\chi)$. For visual clarity, the horizontal axis is plotted using the transformed coordinate $\log_{10}(1+\chi)$, with tick labels indicating the corresponding values of χ; the BSV point is shown separately as the endpoint. The horizontal dashed lines mark the selected ATI energies E_k used for the energy-resolved trend and endpoint scaling analysis in figure 4. The driving pulse has a central wavelength of 400 nm and a duration of four optical cycles. The BSV limit corresponds to $\chi \to \infty$.

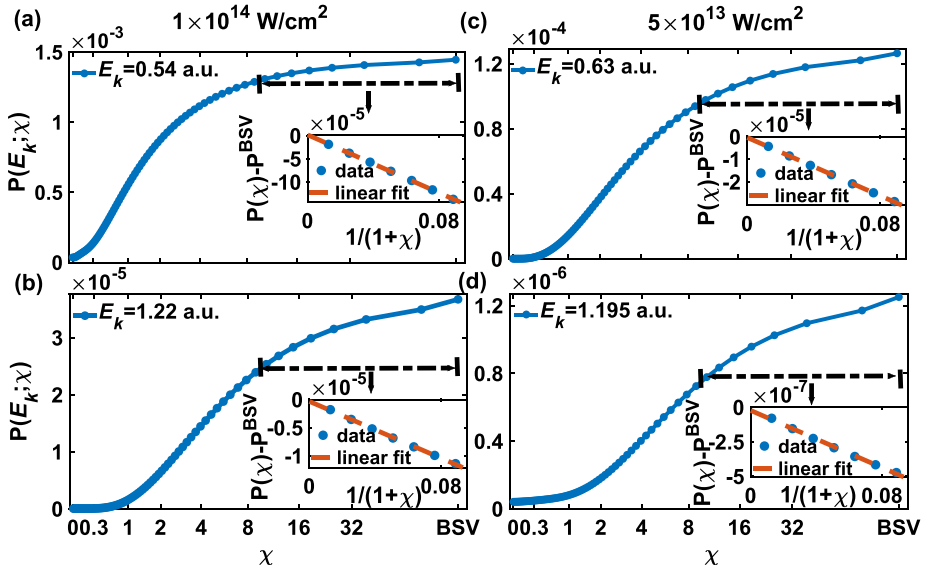


Figure 4. Selected ATI energy signals as a function of the relative squeezing ratio χ and their near-BSV endpoint scaling. (a) and (b) show the selected ATI energies marked in figure 3(a) for $I = 1 \times 10^{14}\,\mathrm{W\,cm^{-2}}$; (c) and (d) show those marked in figure 3(b) for $I = 5 \times 10^{13}\,\mathrm{W\,cm^{-2}}$. For visual clarity, the main horizontal axis is plotted using the transformed coordinate $\log_{10}(1+\chi)$, with tick labels indicating the corresponding values of χ; the BSV point is shown separately as the endpoint. The insets show $P(E_k;\chi) - P(E_k;\mathrm{BSV})$ as a function of $1/(1+\chi)$. Dashed lines denote linear fits in the near-BSV region. The driving pulse has a central wavelength of 400 nm and a duration of four optical cycles. The BSV limit corresponds to $\chi \to \infty$.

shown in our recent study of electron dynamics under coherent, SC, and BSV driving, the probability flow of the released electron becomes progressively more dispersed and the associated trajectories become less synchronized as the coherent component is reduced [26].

3.2. Quadrature-space interpretation of the transition and endpoint scaling

We now interpret these transition features from the field-quadrature perspective. The numerical results above reveal two common features. First, the total ionization yield and the selected ATI energy signals

change rapidly at smaller χ and then vary more gradually as the BSV limit is approached. Second, their deviations from the BSV values become approximately linear functions of $1/(1+\chi)$ near the endpoint. In the following, we show that the rapid-to-slow variation can be naturally understood from the decreasing rates of change of the Gaussian center and width along the fixed-N path, whereas the endpoint scaling follows from a local expansion around the BSV point, where parity symmetry removes the first-order center response and the width variation provides the other leading correction.

Let O denote either the total ionization yield Y_{ion} or the energy-resolved signal $P(E_k)$ at a selected ATI energy E_k. Since the Gaussian wave function in equation (1) depends on the width through σ^2, we use σ^2 as the width variable in the following analysis. We therefore write the observable as $O(\chi) = O[y_0(\chi), \sigma^2(\chi)]$, with

$$O\left(y_0, \sigma^2\right) = \int \mathrm{d}y_1 \mathrm{d}y_2 \, \varphi_{y_0,\sigma}\left(y_1\right) \varphi^*_{y_0,\sigma}\left(y_2\right) K_O\left(y_1, y_2; t_e\right). \tag{11}$$

Here, K_O denotes the corresponding response kernel. At fixed mean photon number N, the Gaussian parameters are $y_0(\chi) = \sqrt{2N/[\omega(1+\chi)]}$ and $\sigma^2(\chi) = \omega^{-1}\exp[-2\,\mathrm{arsinh}\,\sqrt{N_{\mathrm{sq}}}] = \omega^{-1}\exp[-2\,\mathrm{arsinh}\,\sqrt{N\chi/(1+\chi)}]$. Thus, increasing χ reduces the Gaussian center and changes the width toward its BSV value, namely $y_0 \to 0$ and $\sigma \to \sigma_{\mathrm{BSV}}$.

The rate of change of O along this path is

$$\frac{\mathrm{d}O}{d\chi} = \frac{\partial O}{\partial y_0}\frac{\mathrm{d}y_0}{\mathrm{d}\chi} + \frac{\partial O}{\partial \sigma^2}\frac{\mathrm{d}\sigma^2}{\mathrm{d}\chi}. \tag{12}$$

The corresponding derivatives of the Gaussian parameters are

$$\frac{\mathrm{d}y_0}{\mathrm{d}\chi} = -\frac{y_0}{2\left(1+\chi\right)}, \qquad \frac{\mathrm{d}\sigma^2}{\mathrm{d}\chi} = -\sigma^2 \frac{N}{\left(1+\chi\right)^2\sqrt{N_{\mathrm{sq}}\left(1+N_{\mathrm{sq}}\right)}}, \tag{13}$$

where $N_{\mathrm{sq}} = N\chi/(1+\chi)$. The magnitudes of both derivatives decrease as the BSV endpoint is approached. In fact, the Gaussian parameters y_0 and σ^2 become less sensitive to changes in χ near the endpoint. In particular, the width parameter σ^2 undergoes a rapid initial change and then gradually approaches its BSV value. This provides a natural explanation for the rapid-to-slow variation of the observables along the coherent-to-BSV path. The actual rate of change of O is also weighted by the local center and width responses, $\partial O/\partial y_0$ and $\partial O/\partial\sigma^2$. We therefore examine these local responses around the BSV point, starting with the center response constrained by parity symmetry.

For the coupled system, the combined atom-field parity operator is $\hat{\Pi} = \hat{\Pi}_{\mathrm{A}} \otimes \hat{\Pi}_{\mathrm{F}}$. The field-parity operator acts on the quadrature eigenstates as $\hat{\Pi}_{\mathrm{F}}|y\rangle = |-y\rangle$, and the atomic ground state is even, $\hat{\Pi}_{\mathrm{A}}|g\rangle = |g\rangle$. Therefore, $|g,-y\rangle = \hat{\Pi}|g,y\rangle$. In addition, $\hat{\Pi}_{\mathrm{A}}\hat{d}\hat{\Pi}_{\mathrm{A}}^{\dagger} = -\hat{d}$ and $\hat{\Pi}_{\mathrm{F}}\hat{E}\hat{\Pi}_{\mathrm{F}}^{\dagger} = -\hat{E}$. Since $f(t)$ is a function of time and is unchanged under parity, the interaction term $-f(t)\hat{d}\hat{E}$ is invariant under the combined parity transformation. The field-free atomic Hamiltonian and the field Hamiltonian are also parity even. Hence, $\hat{\Pi}\hat{H}(t)\hat{\Pi}^{\dagger} = \hat{H}(t)$ at each time, and the time-ordered propagator commutes with the combined parity operator, $\hat{\Pi}\hat{U}(t_e,0)\hat{\Pi}^{\dagger} = \hat{U}(t_e,0)$[58, 59]. Using equation (5), we then obtain

$$\begin{aligned}
\hat{\mathcal{R}}\left(-y_1,-y_2;t_e\right) &= \mathrm{Tr}_{\mathrm{F}}\left[\hat{U}\left(t_e,0\right)\hat{\Pi}|g,y_1\rangle\langle g,y_2|\hat{\Pi}^{\dagger}\hat{U}^{\dagger}\left(t_e,0\right)\right] \\
&= \hat{\Pi}_{\mathrm{A}}\mathrm{Tr}_{\mathrm{F}}\left[\hat{\Pi}_{\mathrm{F}}\hat{U}\left(t_e,0\right)|g,y_1\rangle\langle g,y_2|\hat{U}^{\dagger}\left(t_e,0\right)\hat{\Pi}_{\mathrm{F}}^{\dagger}\right]\hat{\Pi}_{\mathrm{A}}^{\dagger} \\
&= \hat{\Pi}_{\mathrm{A}}\hat{\mathcal{R}}\left(y_1,y_2;t_e\right)\hat{\Pi}_{\mathrm{A}}^{\dagger}.
\end{aligned} \tag{14}$$

In the last equality, we used the cyclic property of the trace over the field degree of freedom to remove the field-parity operators $\hat{\Pi}_{\mathrm{F}}$ and $\hat{\Pi}_{\mathrm{F}}^{\dagger}$.

The measurement operator $\hat{M}_O$ is also parity even for the observables considered here. For the ionization yield, $\hat{M}_O = \hat{Q}_{\mathrm{B}}$, where $\hat{Q}_{\mathrm{B}} = \hat{I}_{\mathrm{A}} - \hat{P}_{\mathrm{B}}$ and $\hat{P}_{\mathrm{B}}$ projects onto the bound eigenstates of the field-free atomic Hamiltonian. Since the atom is centrosymmetric, $\hat{H}_{\mathrm{A}}$ commutes with the atomic parity operator $\hat{\Pi}_{\mathrm{A}}$. The bound subspace is therefore invariant under $\hat{\Pi}_{\mathrm{A}}$, which gives $\hat{\Pi}_{\mathrm{A}}^{\dagger}\hat{P}_{\mathrm{B}}\hat{\Pi}_{\mathrm{A}} = \hat{P}_{\mathrm{B}}$ and hence $\hat{\Pi}_{\mathrm{A}}^{\dagger}\hat{Q}_{\mathrm{B}}\hat{\Pi}_{\mathrm{A}} = \hat{Q}_{\mathrm{B}}$[59]. For the energy-resolved photoelectron signal evaluated at a selected ATI energy E_k, the measurement operator is $\hat{M}_O = \hat{Q}_{\mathrm{B}}\hat{W}_{E_k}^{(q)}\hat{Q}_{\mathrm{B}}$. The window operator $\hat{W}_{E_k}^{(q)}$ is a function of $\hat{H}_{\mathrm{A}}$ and is

therefore parity even as well. Thus, in both cases, $\hat{\Pi}_{\rm A}^{\dagger}\hat{M}_O\hat{\Pi}_{\rm A}=\hat{M}_O$. Using equation (14), the corresponding response kernel $K_O(y_1,y_2;t_e)={\rm Tr}_{\rm A}[\hat{M}_O\hat{\mathcal{R}}(y_1,y_2;t_e)]$ satisfies

$$\begin{aligned}K_O(-y_1,-y_2;t_e)&={\rm Tr}_{\rm A}\left[\hat{M}_O\hat{\mathcal{R}}(-y_1,-y_2;t_e)\right]\\&={\rm Tr}_{\rm A}\left[\hat{M}_O\hat{\Pi}_{\rm A}\hat{\mathcal{R}}(y_1,y_2;t_e)\hat{\Pi}_{\rm A}^{\dagger}\right]\\&={\rm Tr}_{\rm A}\left[\hat{\Pi}_{\rm A}^{\dagger}\hat{M}_O\hat{\Pi}_{\rm A}\hat{\mathcal{R}}(y_1,y_2;t_e)\right]\\&={\rm Tr}_{\rm A}\left[\hat{M}_O\hat{\mathcal{R}}(y_1,y_2;t_e)\right]\\&=K_O(y_1,y_2;t_e).\end{aligned}\tag{15}$$

Here, the third line follows from the cyclic property of the trace, and the fourth line uses the parity-even property of $\hat{M}_O$.

We now use the symmetry of the Gaussian field wave packet. From the definition $\varphi_{y_0,\sigma}(y)=\left(\pi\sigma^2\right)^{-1/4}\exp\left[-(y-y_0)^2/(2\sigma^2)\right]$, changing the center from y_0 to $-y_0$ gives $\varphi_{-y_0,\sigma}(y)=\varphi_{y_0,\sigma}(-y)=\left(\pi\sigma^2\right)^{-1/4}\exp\left[-(y+y_0)^2/(2\sigma^2)\right]$. Thus, changing the sign of the Gaussian center is equivalent to reflecting the quadrature coordinate. Using the kernel symmetry in equation (15), we obtain

$$\begin{aligned}O\left(-y_0,\sigma^2\right)&=\int{\rm d}y_1{\rm d}y_2\,\varphi_{-y_0,\sigma}(y_1)\,\varphi^{*}_{-y_0,\sigma}(y_2)\,K_O(y_1,y_2;t_e)\\&=\int{\rm d}y_1{\rm d}y_2\,\varphi_{y_0,\sigma}(-y_1)\,\varphi^{*}_{y_0,\sigma}(-y_2)\,K_O(y_1,y_2;t_e)\\&=\int{\rm d}y_1'{\rm d}y_2'\,\varphi_{y_0,\sigma}(y_1')\,\varphi^{*}_{y_0,\sigma}(y_2')\,K_O(-y_1',-y_2';t_e)\\&=\int{\rm d}y_1'{\rm d}y_2'\,\varphi_{y_0,\sigma}(y_1')\,\varphi^{*}_{y_0,\sigma}(y_2')\,K_O(y_1',y_2';t_e)\\&=O\left(y_0,\sigma^2\right).\end{aligned}\tag{16}$$

In the third line, we used the change of variables $y_1'=-y_1$ and $y_2'=-y_2$. Since the integration is over the entire quadrature space, the integration limits are unchanged. Equation (16) shows that O is an even function of the Gaussian center y_0. In particular, the BSV point $y_0=0$ is stationary with respect to center displacement, $\partial O/\partial y_0|_{y_0=0}=0$.

At fixed BSV width, the leading response to a small center displacement is therefore quadratic:

$$O\left(\delta y,\sigma_{\rm BSV}^2\right)-O\left(0,\sigma_{\rm BSV}^2\right)=\frac{1}{2}\left.\frac{\partial^2 O}{\partial y_0^2}\right|_{\rm BSV}(\delta y)^2+\mathcal{O}\left((\delta y)^4\right).\tag{17}$$

Here, the subscript 'BSV' on derivatives denotes evaluation at the BSV point, $y_0=0$ and $\sigma^2=\sigma_{\rm BSV}^2$. This center-displacement response is tested numerically in figure 5 using the ionization yield as an example. Figures 5(a) and (b) examine the response around the BSV point for $I=1\times10^{14}\,{\rm W\,cm^{-2}}$ and $5\times10^{13}\,{\rm W\,cm^{-2}}$, respectively. The Gaussian width is fixed at $\sigma_{\rm BSV}$, and a small center displacement δy is applied around $y_0=0$. The normalized yield variation $[Y(\delta y)-Y(0)]/Y(0)$ is plotted as a function of the dimensionless quantity $(\delta y/y_c)^2$, where y_c denotes the Gaussian center of the coherent state at the same mean photon number. The approximately linear dependence in figures 5(a) and (b) confirms that the leading response at the BSV point is quadratic in δy, consistent with the absence of the first-order term required by parity symmetry.

For comparison, figures 5(c) and (d) show the response around the coherent-state center y_c for the same two intensities. In this case, the width is fixed at the coherent-state value σ_c, and the normalized variation $[Y(y_c+\delta y)-Y(y_c)]/Y(y_c)$ is plotted as a function of the dimensionless displacement $\delta y/y_c$. The nearly linear dependence shows that a first-order center response is generally present when the local expansion is made around a nonzero center such as y_c, in contrast to the expansion around the BSV point, where parity symmetry removes the first-order term. Therefore, figure 5 numerically confirms the parity-induced vanishing of the first-order response to Gaussian-center displacement at the BSV point.

The center-displacement analysis above specifies the factor $\partial O/\partial y_0$ in the center contribution $(\partial O/\partial y_0)({\rm d}y_0/{\rm d}\chi)$ of equation (12). It shows that the response changes from a generally first-order dependence around the coherent-state center to a quadratic dependence at the BSV endpoint. This change complements the path-dependent slowing discussed above. Near the BSV endpoint, for small y_0, the center dependence can be written locally as $O(y_0,\sigma_{\rm BSV}^2)-O(0,\sigma_{\rm BSV}^2)\propto y_0^2$. Taking the derivative with respect to y_0 then gives the local center response entering equation (12), $\partial O/\partial y_0\propto y_0$. Since

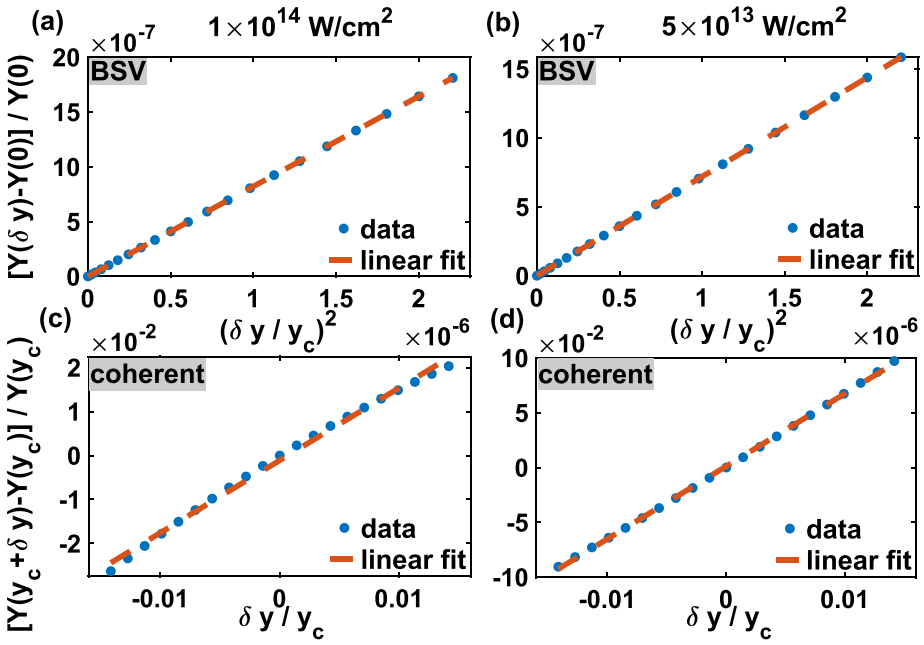


Figure 5. Center-displacement response of the ionization yield near the BSV and coherent-state points. (a) and (b) show the normalized yield variation near the BSV point, $[Y(\delta y) - Y(0)]/Y(0)$, as a function of $(\delta y/y_c)^2$ for $I = 1 \times 10^{14}\,\mathrm{W\,cm^{-2}}$ and $5 \times 10^{13}\,\mathrm{W\,cm^{-2}}$, respectively. (c) and (d) show the normalized yield variation near the coherent-state center, $[Y(y_c + \delta y) - Y(y_c)]/Y(y_c)$, as a function of $\delta y/y_c$ for the same two intensities. Dashed lines denote linear fits. The driving pulse has a central wavelength of 400 nm and a duration of four optical cycles.

along the fixed-N path $y_0(\chi) \propto (1+\chi)^{-1/2}$ and $\mathrm{d}y_0/\mathrm{d}\chi \propto (1+\chi)^{-3/2}$, the center term in equation (12), $(\partial O/\partial y_0)(\mathrm{d}y_0/\mathrm{d}\chi)$, scales as $(1+\chi)^{-2}$ near the endpoint.

The second local contribution comes from the width variation at fixed center $y_0 = 0$. For a smooth observable, its local expansion around the BSV width gives

$$O\left(0,\sigma^2\right) - O\left(0,\sigma^2_{\mathrm{BSV}}\right) = \left.\frac{\partial O}{\partial \sigma^2}\right|_{\mathrm{BSV}} \left(\sigma^2 - \sigma^2_{\mathrm{BSV}}\right) + \mathcal{O}\left(\left(\sigma^2 - \sigma^2_{\mathrm{BSV}}\right)^2\right). \tag{18}$$

This width dependence is tested numerically in figure 6 using the ionization yield as an example. Figures 6(a) and (b) correspond to $I = 1 \times 10^{14}\,\mathrm{W\,cm^{-2}}$ and $5 \times 10^{13}\,\mathrm{W\,cm^{-2}}$, respectively. In both cases, the center is fixed at $y_0 = 0$, and the normalized yield variation $[Y_{\mathrm{ion}}(\sigma^2) - Y_{\mathrm{ion}}(\sigma^2_{\mathrm{BSV}})]/Y_{\mathrm{ion}}(\sigma^2_{\mathrm{BSV}})$ is plotted as a function of the normalized squared-width change $(\sigma/\sigma_{\mathrm{BSV}})^2 - 1$. The approximately linear dependence confirms that the leading width correction near the BSV point is proportional to $\sigma^2 - \sigma^2_{\mathrm{BSV}}$. A similar leading-order dependence was also verified around the coherent-state width, indicating that a first-order width response is not specific to the BSV endpoint. Therefore, the rapid-to-slow variation of the width contribution is largely controlled by the decreasing magnitude of $\mathrm{d}\sigma^2/\mathrm{d}\chi$ along the fixed-N path.

The chain rule in equation (12) accounts for the simultaneous changes of the Gaussian center and width along the fixed-N path. We now evaluate the leading endpoint scaling of the width term. In the near-BSV region, $N_{\mathrm{sq}} = N\chi/(1+\chi)$ is close to N, while $\sigma^2(\chi)$ is close to $\sigma^2_{\mathrm{BSV}} = \omega^{-1}\exp[-2\,\mathrm{arsinh}\sqrt{N}]$. Using these endpoint values in equation (13) and retaining the explicit χ dependence gives $\frac{\mathrm{d}\sigma^2}{\mathrm{d}\chi} \simeq -\sigma^2_{\mathrm{BSV}}\sqrt{N/(1+N)}(1+\chi)^{-2} \propto (1+\chi)^{-2}$. Since the width response is linear in $\sigma^2 - \sigma^2_{\mathrm{BSV}}$ near the BSV point, $\partial O/\partial\sigma^2$ contributes only a constant prefactor to leading order and does not change the χ scaling. Therefore, the width contribution $(\partial O/\partial\sigma^2)(\mathrm{d}\sigma^2/\mathrm{d}\chi)$ to $\mathrm{d}O/\mathrm{d}\chi$ has the same scaling as $\mathrm{d}\sigma^2/\mathrm{d}\chi$, namely $(1+\chi)^{-2}$. Together with the center contribution derived above, both terms in equation (12) therefore contribute to $\mathrm{d}O/\mathrm{d}\chi$ with the same endpoint scaling, $(1+\chi)^{-2}$. Integrating this endpoint behavior from χ toward the BSV endpoint gives

$$O(\chi) - O_{\mathrm{BSV}} \propto \frac{1}{1+\chi}. \tag{19}$$

Equation (19) gives the leading endpoint dependence as the BSV limit is approached. This relation determines only the leading power at the BSV endpoint; it does not specify how far away from the

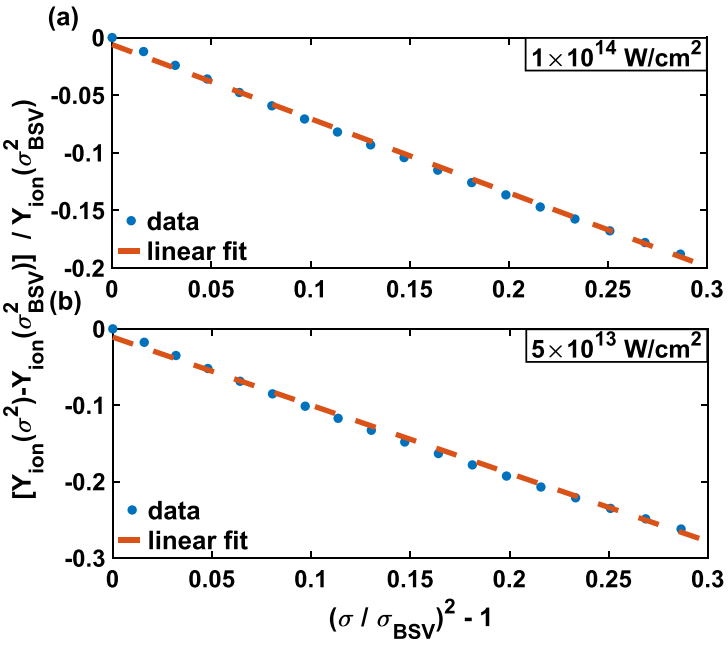


Figure 6. Width response of the ionization yield near the BSV point. (a) and (b) correspond to $I = 1 \times 10^{14}\,\mathrm{W\,cm^{-2}}$ and $5 \times 10^{13}\,\mathrm{W\,cm^{-2}}$, respectively. The Gaussian center is fixed at $y_0 = 0$, while the width σ is varied around σ_{BSV}. The normalized yield variation $[Y_{\mathrm{ion}}(\sigma^2) - Y_{\mathrm{ion}}(\sigma^2_{\mathrm{BSV}})]/Y_{\mathrm{ion}}(\sigma^2_{\mathrm{BSV}})$ is plotted as a function of the normalized squared-width change $(\sigma/\sigma_{\mathrm{BSV}})^2 - 1$. Dashed lines denote fits to the leading-order dependence on $\sigma^2 - \sigma^2_{\mathrm{BSV}}$ near the BSV point. The driving pulse has a central wavelength of 400 nm and a duration of four optical cycles.

endpoint the linear approximation remains quantitatively accurate. More generally, the observable can be expanded as $O(\chi) = O_{\mathrm{BSV}} + C_1/(1+\chi) + C_2/(1+\chi)^2 + \cdots$, where the coefficients C_j contain the detailed atom-, pulse-, and observable-dependent responses. The approximately linear behavior observed numerically over a broader range of $1/(1+\chi)$ indicates that the higher-order corrections are comparatively small for the systems and pulse parameters considered here. Thus, the extent of this finite-range linear behavior is system dependent, whereas the leading endpoint power follows from the symmetry and smoothness arguments above. We next discuss the applicability of this scaling and its possible diagnostic implication.

4. Applicability and experimental implications

4.1. Applicability of the near-bright squeezed vacuum (BSV) scaling

The above derivation and conclusion are not tied to the one-dimensional model used here to provide numerical tests. The calculations presented, including the total ionization yield and energy-resolved photoelectron spectra, provide illustrative examples of the local symmetry-based scaling. More advanced one-dimensional atomic model potentials can improve quantitative agreement with three-dimensional strong-field calculations [60–62]. Here, the soft-core potential is used as a simple inversion-symmetric model for testing the symmetry-based endpoint scaling. As shown in equation (12), the dependence on χ enters through the Gaussian center $y_0(\chi)$ and squared width $\sigma^2(\chi)$, whereas the detailed atom- and pulse-dependent response is contained in $\partial O/\partial y_0$ and $\partial O/\partial\sigma^2$. The parity relation in equation (16) removes the first-order center response and makes the leading allowed center correction quadratic near the BSV point. This quadratic center structure applies whenever the matter system is inversion symmetric, its initial state has definite parity, the coupled light–matter Hamiltonian is invariant under the combined parity transformation, and the measured observable is parity even. None of these conditions is specific to the spatial dimensionality of the atomic model. The laser wavelength, pulse duration, and pulse envelope likewise do not alter these symmetry conditions and therefore do not change the leading endpoint power. Under these symmetry conditions, reversing the Gaussian center does not change the observable. Moreover, the leading width correction in equation (18) follows from a local Taylor expansion around σ^2_{BSV} and does not require an additional symmetry. The same reasoning applies to the opposite squeezing sign, since the parity argument depends only on the vanishing Gaussian center at the BSV point and not on which quadrature is squeezed. The same symmetry-based argument can

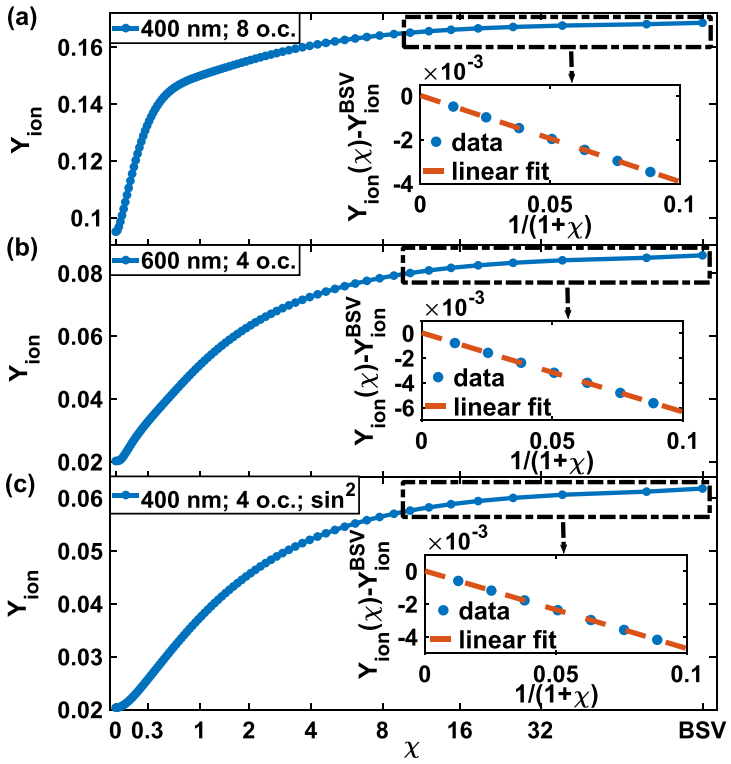


Figure 7. Total ionization yield as a function of the relative squeezing ratio χ along the coherent-to-BSV transition at fixed mean photon number for three sets of laser parameters. The laser intensity is $5 \times 10^{13}\mathrm{W\,cm^{-2}}$ in all panels. (a) A 400-nm, eight-cycle trapezoidal pulse with a two-cycle ramp-on, a four-cycle plateau, and a two-cycle ramp-off. (b) A 600-nm, four-cycle trapezoidal pulse with a one-cycle ramp-on, a two-cycle plateau, and a one-cycle ramp-off. (c) A 400-nm, four-cycle pulse with a $\sin^2$ envelope. The insets show the near-BSV deviation $Y_{\mathrm{ion}}(\chi) - Y_{\mathrm{ion}}^{\mathrm{BSV}}$ plotted as a function of $1/(1+\chi)$. Dashed lines denote linear fits in the endpoint region.

be generalized to fixed-phase complex coherent and squeezing parameters, although the response coefficients may depend on the corresponding phases. Together with the χ dependence of the center and width given in equation (13), these properties lead to the near-BSV scaling $O(\chi) - O_{\mathrm{BSV}} \propto 1/(1+\chi)$. The robustness of this endpoint dependence against changes in the laser parameters is tested numerically in figure 7. The figure compares the total ionization yield for different wavelengths, pulse durations, and pulse envelopes while keeping the laser intensity and mean photon number fixed. Although the overall ionization yields and the slopes of the near-endpoint responses depend on the laser parameters, the insets show that $Y_{\mathrm{ion}}(\chi) - Y_{\mathrm{ion}}^{\mathrm{BSV}}$ remains linear in $1/(1+\chi)$ near the BSV endpoint in all three cases.

4.2. Experimental implications for residual-coherence diagnostics

We next consider a possible experimental implication of the near-BSV analysis. Ideally, BSV generated by an unseeded high-gain parametric process has no first-order coherent amplitude, $\langle \hat{a} \rangle = 0$[39, 63, 64]. In practice, however, weak coherent background fields at the signal frequency may be introduced by residual leakage of calibration or auxiliary beams, or by other mode-matched parasitic signal-frequency fields in the optical path. The mode-matched and phase-stable part of this background acts as a residual coherent component in the optical mode that interacts with the atom [65, 66]. The resulting state is more appropriately described as a SC state rather than an ideal squeezed vacuum [67]. This issue is particularly relevant for BSV, for which direct homodyne measurement of the squeezed quadrature can be experimentally challenging, so the squeezing strength is often inferred from the measured photon number [68]. A mean photon-number measurement alone, however, cannot distinguish squeezed photons from a weak residual coherent component occupying the same effective mode.

Along the fixed-mean-photon-number path, $s \equiv (1+\chi)^{-1} = N_{\mathrm{coh}}/(N_{\mathrm{coh}} + N_{\mathrm{sq}})$ is the coherent photon fraction. The near-BSV scaling makes the leading response deviation linear in this fraction. A weak residual coherent component with real parameter α_0 contributes $N_{\mathrm{coh}} = \alpha_0^2$ and shifts the Gaussian center as $y_0 \propto \alpha_0$. At fixed BSV width, equation (17) then gives $O - O_{\mathrm{BSV}} \propto y_0^2 \propto \alpha_0^2$. This relation suggests a response-based diagnostic in which a weak, mode-matched coherent field is applied along the same real quadrature and the resulting change in the ionization response is monitored, rather than relying on a direct optical quadrature measurement.

5. Conclusion

We have formulated strong-field ionization by squeezed light in field-quadrature space, where coherent, SC, and BSV states become a continuous family of Gaussian wave packets. This description represents the fixed-N coherent-to-BSV transition as a continuous evolution of the Gaussian center and width.

The central result is that BSV is a symmetry-protected endpoint: combined parity forbids the linear response of a parity-even observable to residual coherent displacement. For a smooth response, the resulting quadratic center correction and the leading width correction both generate $O(\chi) - O_{\mathrm{BSV}} \propto (1+\chi)^{-1}$ along the fixed-N path. Calculations for a one-dimensional soft-core atom confirm this endpoint law for the total yield and ATI channels and explain the observed rapid-to-slow crossover through the decreasing variations of the Gaussian parameters. Within the stated symmetry, smoothness, and mode-matching conditions, the scaling offers a quantitative criterion for approaching BSV and a possible probe of residual mode-matched coherent displacement.

Acknowledgments

This work was supported by NSFC Grants Nos. U2330401, 12474484, 12688201, 12274384, and 12450404.

Data availability statement

The data that support the findings of this study are openly available at the following URL/DOI: https://doi.org/10.6084/m9.figshare.33235842 [69].

ORCID iDs

Haoyu Liu 0009-0000-5985-0163
Jianmin Yuan 0000-0002-9315-0854
Xu Wang 0000-0002-8043-7135

References

[1] Voronov G S and Delone N B 1965 Ionization of the xenon atom by the electric field of ruby laser emission *Sov. JETP Lett.* **1** 66
[2] Voronov G S and Delone N B 1966 Many-photon ionization of the xenon atom by ruby laser radiation *Sov. Phys. JETP* **23** 54–58
[3] Agostini P, Barjot G, Bonnal J, Mainfray G, Manus C and Morellec J 1968 Multiphoton ionization of hydrogen and rare gases *IEEE J. Quantum Electron* **4** 667–9
[4] Agostini P, Fabre F, Mainfray G, Petite G and Rahman N K 1979 Free-free transitions following six-photon ionization of xenon atoms *Phys. Rev. Lett.* **42** 1127
[5] Kruit P, Kimman J, Muller H G and van der Wiel M J 1983 Electron spectra from multiphoton ionization of xenon at 1064, 532 and 355 nm *Phys. Rev. A* **28** 248–55
[6] Paulus G G, Nicklich W, Xu H, Lambropoulos P and Walther H 1994 Plateau in above threshold ionization spectra *Phys. Rev. Lett.* **72** 2851–4
[7] Keldysh L V 1965 Ionization in the field of a strong electromagnetic wave *Sov. Phys. JETP* **20** 1307–14
[8] Faisal F H M 1973 Multiple absorption of laser photons by atoms *J. Phys. B: At. Mol. Phys.* **6** L89–L92
[9] Reiss H R 1980 Effect of an intense electromagnetic field on a weakly bound system *Phys. Rev. A* **22** 1786
[10] Ammosov M V, Delone N B and Krainov V P 1986 Tunnel ionization of complex atoms and atomic ions in electromagnetic field *High Intensity Laser Processes* **vol 664** pp 138–41
[11] Kulander K C, Schafer K J and Krause J L 1993 Dynamics of short-pulse excitation, ionization and harmonic conversion *Super-Intense Laser-Atom Physics* (Springer) p 95
[12] Schafer K J, Yang B, DiMauro L F and Kulander K C 1993 Above threshold ionization beyond the high harmonic cutoff *Phys. Rev. Lett.* **70** 1599
[13] Corkum P B 1993 Plasma perspective on strong field multiphoton ionization *Phys. Rev. Lett.* **71** 1994
[14] Iskhakov T, Pérez A M, Spasibko K, Chekhova M V and Leuchs G 2012 Superbunched bright squeezed vacuum state *Opt. Lett.* **37** 1919
[15] Spasibko K, Kopylov D, Krutyanskiy V, Murzina T, Leuchs G and Chekhova M 2017 Multiphoton effects enhanced due to ultrafast photon-number fluctuations *Phys. Rev. Lett.* **119** 223603
[16] Manceau M, Spasibko K, Leuchs G, Filip R and Chekhova M 2019 Indefinite-mean Pareto photon distribution from amplified quantum noise *Phys. Rev. Lett.* **123** 123606
[17] Rasputnyi A, Chen Z, Birk M, Cohen O, Kaminer I, Krüger M, Seletskiy D, Chekhova M and Tani F 2024 High-harmonic generation by a bright squeezed vacuum *Nat. Phys.* **20** 1960
[18] Lemieux S, Jalil S A, Purschke D N, Boroumand N, Hammond T J, Villeneuve D, Naumov A, Brabec T and Vampa G 2025 Photon bunching in high-harmonic emission controlled by quantum light *Nat. Photon.* **19** 767

[19] Tzur M E *et al* 2025 Attosecond-resolved quantum fluctuations of light and matter (arXiv:2511.18362)
[20] Heimerl J, Mikhaylov A, Meier S, Höllerer H, Kaminer I, Chekhova M and Hommelhoff P 2024 Multiphoton electron emission with non-classical light *Nat. Phys.* **20** 945
[21] Heimerl J, Rasputnyi A, Pölloth J, Meier S, Chekhova M and Hommelhoff P 2025 Quantum light drives electrons strongly at metal needle tips *Nat. Phys.* **21** 1899
[22] Jiang Z *et al* 2026 Nonlinear atomic tunnelling boosted by bright squeezed vacuum *Nature* **654** 356–60
[23] Tzur M E, Birk M, Gorlach A, Krüger M, Kaminer I and Cohen O 2023 Photon-statistics force in ultrafast electron dynamics *Nat. Photon.* **17** 501
[24] Tzur M E and Cohen O 2024 Motion of charged particles in bright squeezed vacuum Light *Sci. Appl.* **13** 41
[25] Piazza A D and Qu K 2026 Control of nonlinear Compton scattering in a squeezed vacuum *Phys. Rev. Lett.* **136** 085001
[26] Liu H, Yuan J and Wang X 2026 Electron recollision with bright squeezed vacuum light *J. Phys. B: At. Mol. Opt. Phys.* **59** 175601
[27] Fang Y, Sun F X, He Q and Liu Y 2023 Strong-field ionization of hydrogen atoms with quantum light *Phys. Rev. Lett.* **130** 253201
[28] Wang S and Lai X 2023 High-order above-threshold ionization of an atom in intense quantum light *Phys. Rev. A* **108** 063101
[29] Lyu Z, Sun F, Fang Y, He Q and Liu Y 2025 Effect of photon quantum statistics on electrons in above-threshold ionization *Phys. Rev. Res.* **7** L012072
[30] Liu H, Zhang H, Wang X and Yuan J 2025 Atomic double ionization with quantum light *Phys. Rev. Lett.* **134** 123202
[31] Habibović D and Milošević D B 2025 Intensity-dependent enhancements in strong-field ionization by quantum light *Phys. Rev. A* **112** L051103
[32] Habibović D and Milošević D B 2026 High-order above-threshold ionization by squeezed coherent light *Phys. Rev. A* **113** 043124
[33] Gorlach A, Tzur M E, Birk M, Krüger M, Rivera N, Cohen O and Kaminer I 2023 High-harmonic generation driven by quantum light *Nat. Phys.* **19** 1689
[34] Gothelf R V, Lange C S and Madsen L B 2025 High-order harmonic generation in a crystal driven by quantum light *Phys. Rev. A* **111** 063105
[35] Rivera-Dean J, Stammer P, Ciappina M and Lewenstein M 2025 Structured squeezed light allows for high-harmonic generation in classical forbidden geometries *Phys. Rev. Lett.* **135** 013801
[36] Liu H, Zhang H, Wang X and Yuan J 2026 Theory of high-harmonic generation with quantum light *Phys. Rev. Res.* **8** 023326
[37] Wang S, Yu S, Lai X and Liu X 2024 High harmonic generation from an atom in a squeezed-vacuum environment *Phys. Rev. Res.* **6** 033010
[38] Scully M O and Zubairy M S 1997 *Quantum Optics* (Cambridge University Press)
[39] Grynberg G, Aspect A and Fabre C 2010 *Introduction to Quantum Optics: From the Semi-Classical Approach to Quantized Light* (Cambridge University Press)
[40] Gerry C C and Knight P L 2023 *Introductory Quantum Optics* (Cambridge University Press)
[41] Carmichael H J 2013 *Statistical Methods in Quantum Optics 1: Master Equations and Fokker-Planck Equations* (Springer)
[42] Loudon R and Knight P L 1987 Squeezed light *J. Mod. Opt.* **34** 709–59
[43] Kim M S, de Oliveira F A M and Knight P L 1989 Properties of squeezed number states and squeezed thermal states *Phys. Rev. A* **40** 2494–503
[44] Stammer P, Rivera-Dean J, Maxwell A S, Lamprou T, Argüello-Luengo J, Tzallas P, Ciappina M F and Lewenstein M 2024 Entanglement and squeezing of the optical field modes in high harmonic generation *Phys. Rev. Lett.* **132** 143603
[45] Rivera-Dean J, Crispin H, Stammer P, Lamprou T, Pisanty E, Krüger M, Tzallas P, Lewenstein M and Ciappina M 2024 Squeezed states of light after high-order harmonic generation in excited atomic systems *Phys. Rev. A* **110** 063118
[46] Lange C S, Hansen T and Madsen L B 2024 Electron-correlation-induced nonclassicality of light from high-order harmonic generation *Phys. Rev. A* **109** 033110
[47] Hack S, Czirják A and Földi P 2026 A continuous-mode quantum-optical representation of finite strong-field laser pulses in free space (arXiv:2609.01157)
[48] Hack S, Pusztai B G, Joós K, Varró S, Czirják A and Földi P 2026 Wave packet motion in a quantized electromagnetic field: Analytic results *New J. Phys.* **28** 074510
[49] Schafer K J and Kulander K C 1990 Energy analysis of time-dependent wave functions: Application to above-threshold ionization *Phys. Rev. A* **42** 5794–7
[50] Schafer K J 1991 The energy analysis of time-dependent numerical wave functions *Comput. Phys. Commun.* **63** 427–34
[51] Fetić B, Becker W and Milošević D B 2020 Extracting photoelectron spectra from the time-dependent wave function: Comparison of the projection onto continuum states and window-operator methods *Phys. Rev. A* **102** 023101
[52] Javanainen J, Eberly J H and Su Q 1988 Numerical simulations of multiphoton ionization and above-threshold electron spectra *Phys. Rev. A* **38** 3430
[53] Su Q and Eberly J H 1991 Model atom for multiphoton physics *Phys. Rev. A* **44** 5997
[54] Tsatrafyllis N *et al* 2019 Quantum optical signatures in a strong laser pulse after interaction with semiconductors *Phys. Rev. Lett.* **122** 193602
[55] de-la-Pena S, Neufeld O, Even Tzur M, Cohen O, Appel H and Rubio A 2025 Quantum electrodynamics in high-harmonic generation: Multitrajectory Ehrenfest and exact quantum analysis *J. Chem. Theory Comput.* **21** 283
[56] Mao Y-J, Zhou E-R, Li Y, He P-L and He F 2025 Benchmarking atomic ionization driven by strong quantum light (arXiv:2512.15458)
[57] Fox M 2006 *Quantum Optics: An Introduction* (Oxford University Press)
[58] Cohen-Tannoudji C, Diu B and Laloë F 2019 *Quantum Mechanics, Volume 1: Basic Concepts, Tools and Applications* 2nd edn (Wiley)
[59] Sakurai J J and Napolitano J 2020 *Modern Quantum Mechanics* 3rd edn (Cambridge University Press)
[60] Majorosi S, Benedict M G and Czirják A 2018 Improved one-dimensional model potentials for strong-field simulations *Phys. Rev. A* **98** 023401
[61] Sallai K, Hack S, Majorosi S and Czirják A 2024 One-dimensional model potentials optimized for the calculation of high-order-harmonic-generation spectra *Phys. Rev. A* **110** 063117
[62] Sallai K, Hack S, Majorosi S, Földi P and Czirják A 2026 Chirp- and CEP-dependence of HHG spectra simulated by an upgraded one-dimensional atomic model potential *Phys. Scr.* **101** 355406
[63] Pérez A M, Iskhakov T S, Sharapova P, Lemieux S, Tikhonova O V, Chekhova M V and Leuchs G 2014 Bright squeezed-vacuum source with 1.1 spatial mode *Opt. Lett.* **39** 2403–6

[64] Kern Y, Nisim I, Birk M, Rasputnyi A, Behar D, Chen Z, Kaminer I, Sidorenko P, Cohen O and Krüger M 2026 Single-shot pulse retrieval of femtosecond bright squeezed vacuum *Optica* **13** 395–9
[65] Bromage J, Rothhardt J, Hädrich S, Dorrer C, Jocher C, Demmler S, Limpert J, Tünnermann A and Zuegel J D 2011 Analysis and suppression of parasitic processes in noncollinear optical parametric amplifiers *Opt. Express* **19** 16797–808
[66] Kuznetsov N, Nardi A, Riemensberger J, Davydova A, Churaev M, Seidler P and Kippenberg T J 2025 An ultra-broadband photonic-chip-based parametric amplifier *Nature* **639** 928–34
[67] Young S M and Soh D 2025 Fundamental limits to the generation of highly displaced bright squeezed light using linear optics and parametric amplifiers *Phys. Rev. Res.* **7** 013130
[68] Lyu Z, Du S, Li J, Liu H, Sun F, He Q, Ciappina M and Liu Y 2026 Generation of single-mode and multimode bright squeezed vacuum above 10^{14} photons *Ultrafast Sci.* **6** 0175
[69] Liu H 2026 A Field-Quadrature Perspective on Strong-Field Ionization with Squeezed Light figshare (https://doi.org/10.6084/m9.figshare.33235842.v1)